Paleoceanography and Paleoclimatology

Supporting Information for

Early-Pleistocene orbital variability in Northwest Australian shelf sediments

Song Zhao[1], Katharine M. Grant[1], David Heslop[1], and Stephen Gallagher[2]

[1] Research School of Earth Sciences, Australian National University, Canberra, ACT, Australia.

[2] School of Geography, Earth and Atmospheric Sciences, University of Melbourne, Melbourne, Victoria, Australia.

Contents of this file

Text S1. Alternative eccentricity tunings

In order to fully consider the uncertainty of this eccentricity tuning, twelve scenarios have been found based on different options for each tie-point (Figure S5; Table S4). Pearson and Spearman correlation coefficients are calculated to show the linear and monotonic relationship between eccentricity and our $CaCO_3$ record (Figure S5). Correlation analyses suggest that 53.62, 71.57, 79.97 and 109.18 mbsf are the best four tie-points for the eccentricity minima at 1682, 2066, 2388 and 2821 kyr, respectively (Figure S5k; Table S4). Additionally, we have calculated the corresponding p value for each of the regressions in twelve scenarios to test if there is a more robust relationship between eccentricity and the U1464 $CaCO_3$ record.

Following previous studies (Santer et al., 2000), we estimate residuals in $CaCO_3$ based on the least squares linear regression with eccentricity (i.e., $e(x) = y(x) - \bar{y}(x)$, where e is the regression residual, y is the $CaCO_3$ and $\bar{y}$ is the regression of $CaCO_3$ (dependent variable) with eccentricity (independent variable), x is the eccentricity), and assess the autocorrelation in the residuals. We adjust the effective number of samples according to the autocorrelation and then calculate the p value. Basically, we first calculate the lag-1 autocorrelation coefficient of residuals (r_1) to obtain the effective number of samples (n_e) based on $n_e = n_t * (1 - r_1) / (1 + r_1)$, where n_t is the total number of samples. The variance of residuals (S_e^2) is given by $[1 / (n_e - 2)] * \sum_{n=1}^{nt} e(x)^2$, and the standard error of regression coefficient (b) is defined as $S_b = S_e / [\sum_{n=1}^{nt}(x - \bar{x})^2]^{1/2}$, where $\bar{x}$ is the eccentricity mean. Accordingly, the ratio between b and S_b can be used as the t value, and then substituted to the cumulative t-distribution with $n_e - 2$ degrees of freedom to get p values. The p value for option (k) is smallest one (Figure S5k), which corresponds with its highest correlation coefficients.

Text S2. Uncertainties in IODP Site U1464 dust proxy records

To quantify the potential influence of measurement uncertainties on the observed variability in our dust-flux proxy records, we calculate measurement uncertainties and their propagation in our Log(Zr/Rb), Log(Zr/Fe) and $CaCO_3$-free $IRM_{1T@AF\ 170mT}$ records. The principal formulas for error propagation in this study are as follows (Taylor, 1997):

(i) If q is any function of several variables x, …, z, then $\delta q = \text{sqrt}\ ((\frac{\partial q}{\partial x} * \delta x)^2 + \ldots + (\frac{\partial q}{\partial z} * \delta z)^2)$, where variables x, …, z are measured with one standard deviation (1δ, expressed as δx, …, δz).

(ii) If q is the sum and difference, $q = x + \ldots + z - (u + \ldots + w)$, then $\delta q = \text{sqrt}\ ((\delta x)^2 + \ldots + (\delta z)^2 + (\delta u)^2 + \ldots + (\delta w)^2)$.

(iii) If q = Bx, where B is a known constant, then δq = |B|δx, where |B| is absolute value.

(iv) If q is the product and quotient, $q = (x * \ldots * z) / (u * \ldots * w)$, then $\frac{\delta q}{|q|} = \text{sqrt}\ ((\frac{\delta x}{x})^2 + \ldots + (\frac{\delta z}{z})^2 + (\frac{\delta u}{u})^2 + \ldots + (\frac{\delta w}{w})^2)$.

Based on equation (i), the 1δ of logarithm function (Log(x/y)) can be derived as follows: $\delta\text{Log}(x/y) = \text{sqrt}\ ((\frac{1}{x} * \delta x)^2 + (-\frac{1}{y} * \delta y)^2)$. In this study, the average fractional uncertainties (ratios of 1δ values to values of individual measurement) for Zr, Rb and Fe ($\frac{\delta Zr}{Zr}$, $\frac{\delta Rb}{Rb}$ and $\frac{\delta Fe}{Fe}$) are 0.033, 0.102 and 0.007, respectively. Accordingly, $\delta\text{Log}(Zr/Rb) = \text{sqrt}\ ((\frac{1}{Zr} * \delta Zr)^2 + (-\frac{1}{Rb} * \delta Rb)^2) = \text{sqrt}\ (0.033^2 + 0.102^2) = 0.107$; $\delta\text{Log}(Zr/Fe) = \text{sqrt}\ ((\frac{1}{Zr} * \delta Zr)^2 + (-\frac{1}{Fe} * \delta Fe)^2) = \text{sqrt}\ (0.033^2 + 0.007^2) = 0.034$. To obtain the 1δ of the n-point running average of Log(x/y), equations (ii) and (iii) are applied to divide the δLog(x/y) value by sqrt (n), where n is the number of data-points in the running average; i.e., $\delta\text{Log}(x/y)_{average} = (1/n) * \text{sqrt}\ ((\delta\text{Log}(x/y)_1)^2 + \ldots + (\delta\text{Log}(x/y)_n)^2) = (1/n) * \text{sqrt}\ (n * (\delta\text{Log}(x/y))^2) =$

δLog(x/y) / sqrt (n), where each δLog(x/y) is the same. We use a 21-point running average, which yields $\delta Log(Zr/Rb)_{average}$ = 0.107 / sqrt(21) = 0.023 and $\delta Log(Zr/Fe)_{average}$ = 0.034 / sqrt(21) = 0.007. We further multiply ±1δ values by 1.96 (2.58) to obtain the 95 % (99 %) confidence intervals for Log(Zr/Rb) and Log(Zr/Fe) (Figure S10).

For the $CaCO_3$-free $IRM_{1T@AF\ 170mT}$, we only consider the measurement uncertainty of $CaCO_3$ and its propagation, since the measurement uncertainty of $IRM_{1T@AF\ 170mT}$ is so small that it is effectively negligible in this study. The predicted $CaCO_3$ (fractional value) is calculated by 0.096 * Ln(Ca/Fe) + 0.474, where the average fractional uncertainties of Ca and Fe ($\frac{\delta Ca}{Ca}$ and $\frac{\delta Fe}{Fe}$) are 0.002 and 0.007, respectively. The δLn(Ca/Fe) = sqrt (0.002^2 + 0.007^2) = 0.007, and the $\delta CaCO_3$ = 0.096 * δLn(Ca/Fe) = 0.001, following equation (iii). The $\delta CaCO_3$ can be considered as the δ(1- [$CaCO_3$]) based on equation (iii), and then the fractional uncertainty of (1- [$CaCO_3$]) (i.e., $\frac{\delta(1-[CaCO3])}{(1-[CaCO3])}$) is calculated and can be used as the fractional uncertainty of ([$IRM_{1T@AF\ 170mT}$] / (1- [$CaCO_3$])) (i.e., $\frac{\delta([IRM1T@AF\ 170mT]\ /\ (1-[CaCO3]))}{([IRM1T@AF\ 170mT]\ /\ (1-[CaCO3]))}$) based on equation (iv). Finally, the δ($CaCO_3$-free $IRM_{1T@AF\ 170mT}$), which is δ([$IRM_{1T@AF\ 170mT}$] / (1- [$CaCO_3$])), can be derived to obtain the 95 % (99 %) confidence intervals of $CaCO_3$-free $IRM_{1T@AF\ 170mT}$ using ± 1.96(2.58)δ (Figure S10).

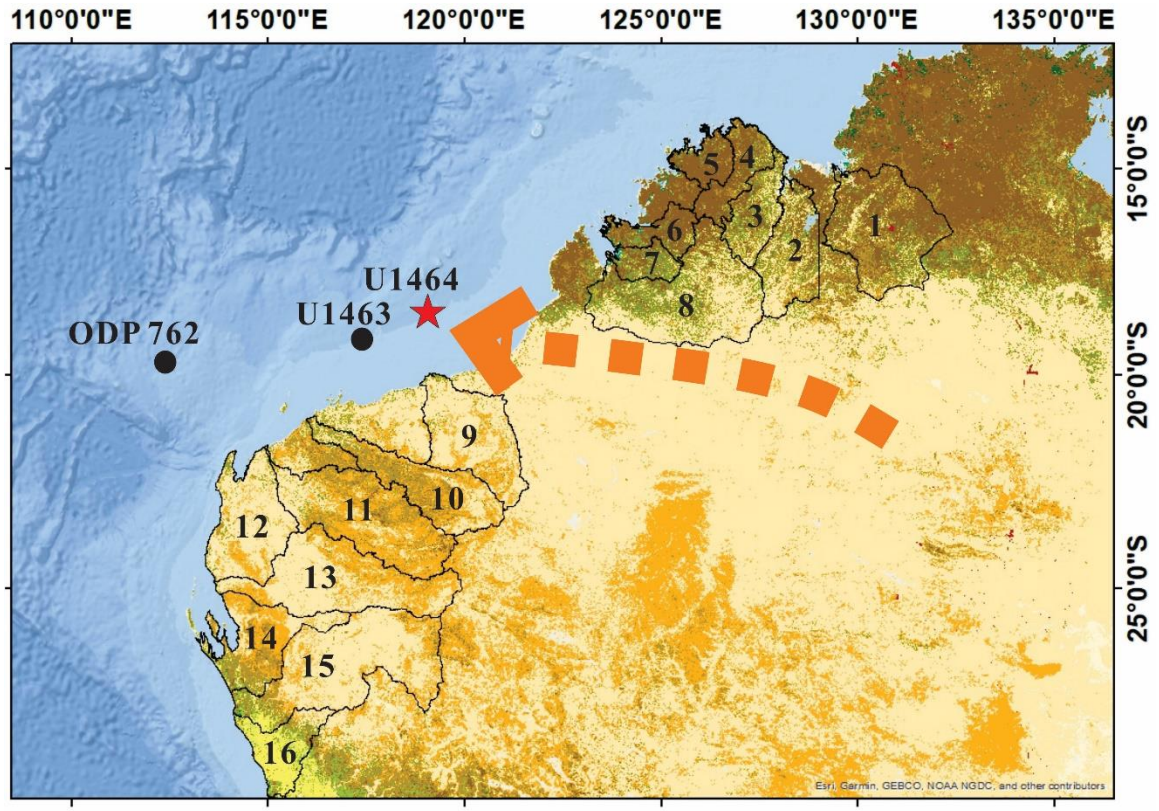

Figure S1. Northwest Australian river basins and locations of three cores (IODP Site U1464, U1463 and ODP site 762). Orange arrow indicates main aeolian dust path (after Bowler, 1976). Drainage basins of Victoria (1), Ord (2), Pentecost (3), Drysdale (4), King Edward (5), Isdell (6), Lennard (7), Fitzroy (8), De Grey (9), Fortescue (10), Ashburton (11), Lyndon-minilya (12), Gascoyne (13), Wooramel (14), Murchison (15), and Greenough (16) rivers (Australia's River Basins, 1997) are marked. Base map is from the GlobCover 2009 land cover and World Ocean Base in ArcGIS online.

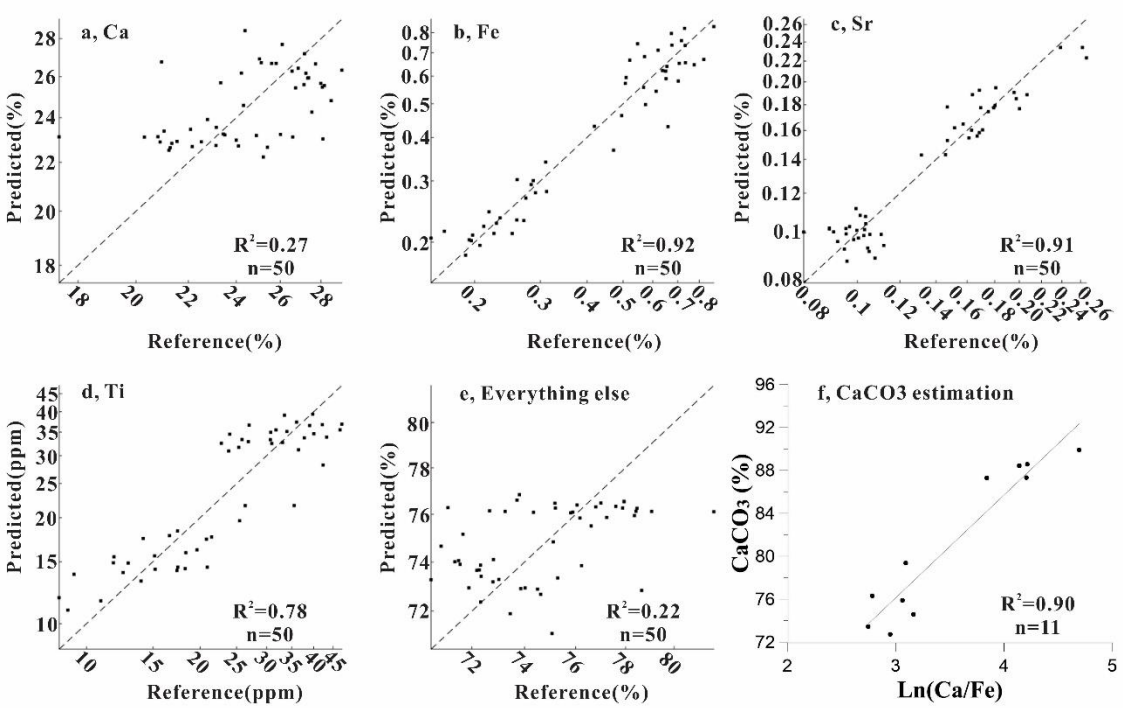

Figure S2. Reference versus predicted element concentrations for IODP Site U1464, based on ICP-OES and scanning XRF (a-e), using a multivariate log-ratio calibration model (Weltje et al., 2015). Shipboard $CaCO_3$ measurements versus Ln(Ca/Fe) for IODP Site U1464 (f) following the method of Liebrand et al., (2016).

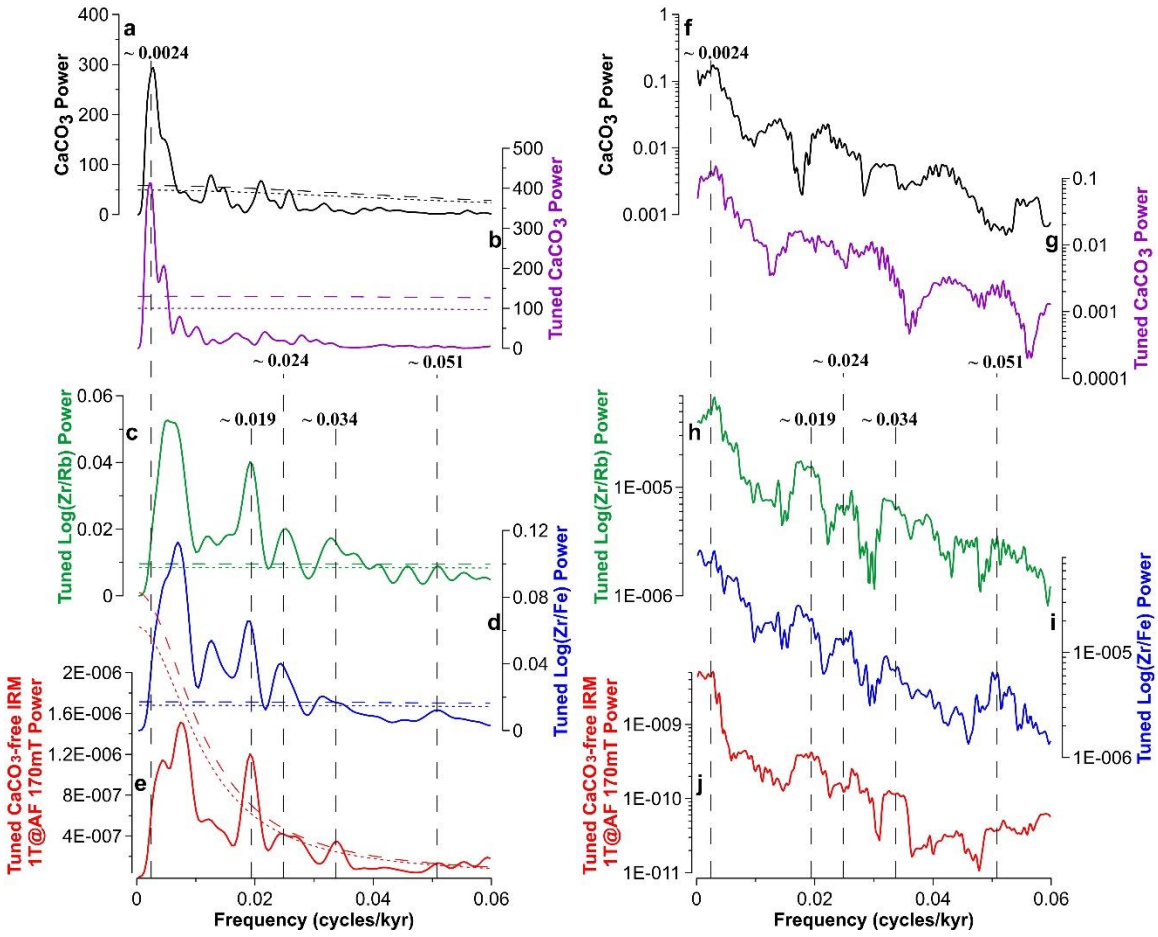

Figure S3. Spectral analyses of Site U1464 proxy records over the 1.6-2.9 Ma interval using the Redfit (a-e) and Multitaper (f-j) methods. Power spectra for $CaCO_3$ (a, f) on the biostratigraphy-based Bayesian model, and $CaCO_3$ (b, g), Log(Zr/Rb) (c, h), Log(Zr/Fe) (d, i) and $CaCO_3$-free $IRM_{1T@AF\ 170mT}$ (e, j) after eccentricity tuning. The a-e represent Redfit spectra with output parameters (oversample = 8, segment = 4 in a-b and oversample = 8, segment = 8 in c-e), and confidence levels (90%, dot; 95%, dashed) are indicated. The f-j represent Multitaper spectra with 5 tapers.

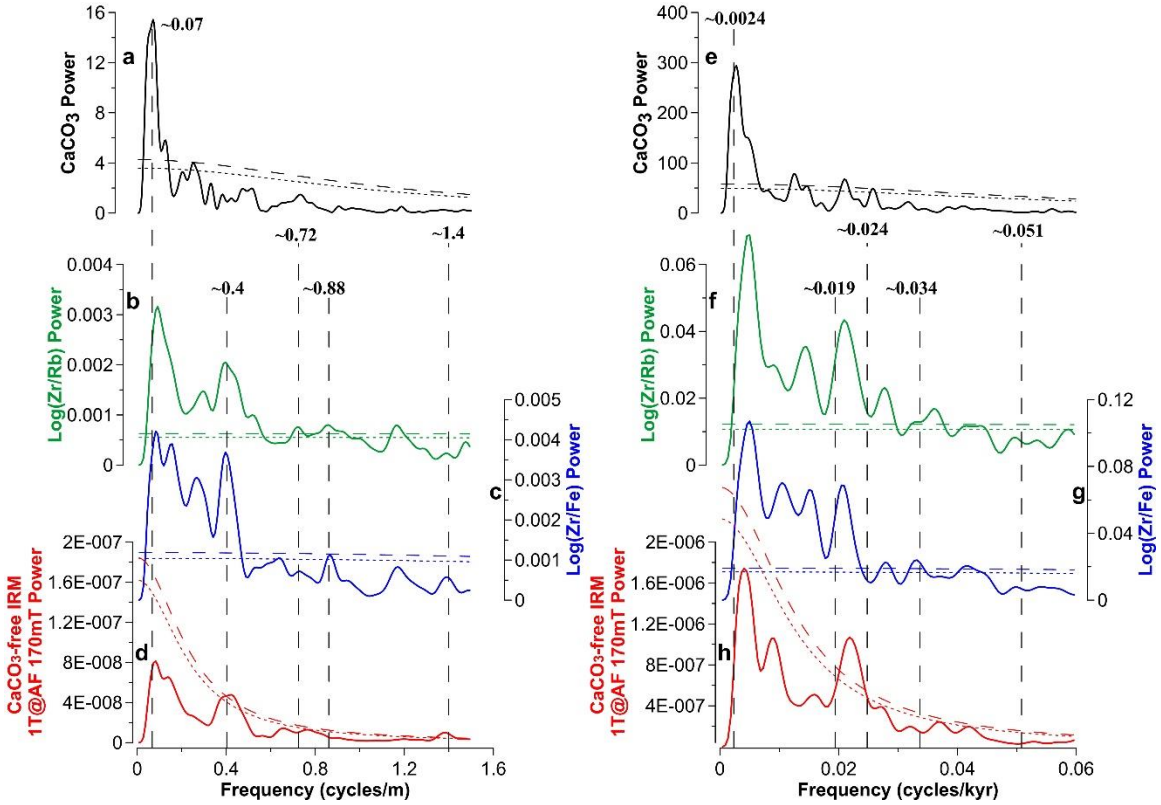

Figure S4. Spectral analyses of Site U1464 proxy records over the interval of ~47-108 mbsf (a-d) or ~1.6-2.9 Ma (e-h) using the Redfit method. Power spectra for $CaCO_3$ (a), Log(Zr/Rb) (b), Log(Zr/Fe) (c) and $CaCO_3$-free $IRM_{1T@AF\ 170mT}$ (d) on depth domain. Power spectra for $CaCO_3$ (e), Log(Zr/Rb) (f), Log(Zr/Fe) (g) and $CaCO_3$-free $IRM_{1T@AF\ 170mT}$ (h) on the biostratigraphy-based Bayesian model. The a-h represent Redfit spectra with output parameters (oversample = 8 and segment = 4 for $CaCO_3$ record; oversample = 8 and segment = 8 for dust proxy records), and confidence levels (90%, dot; 95%, dashed) are indicated.

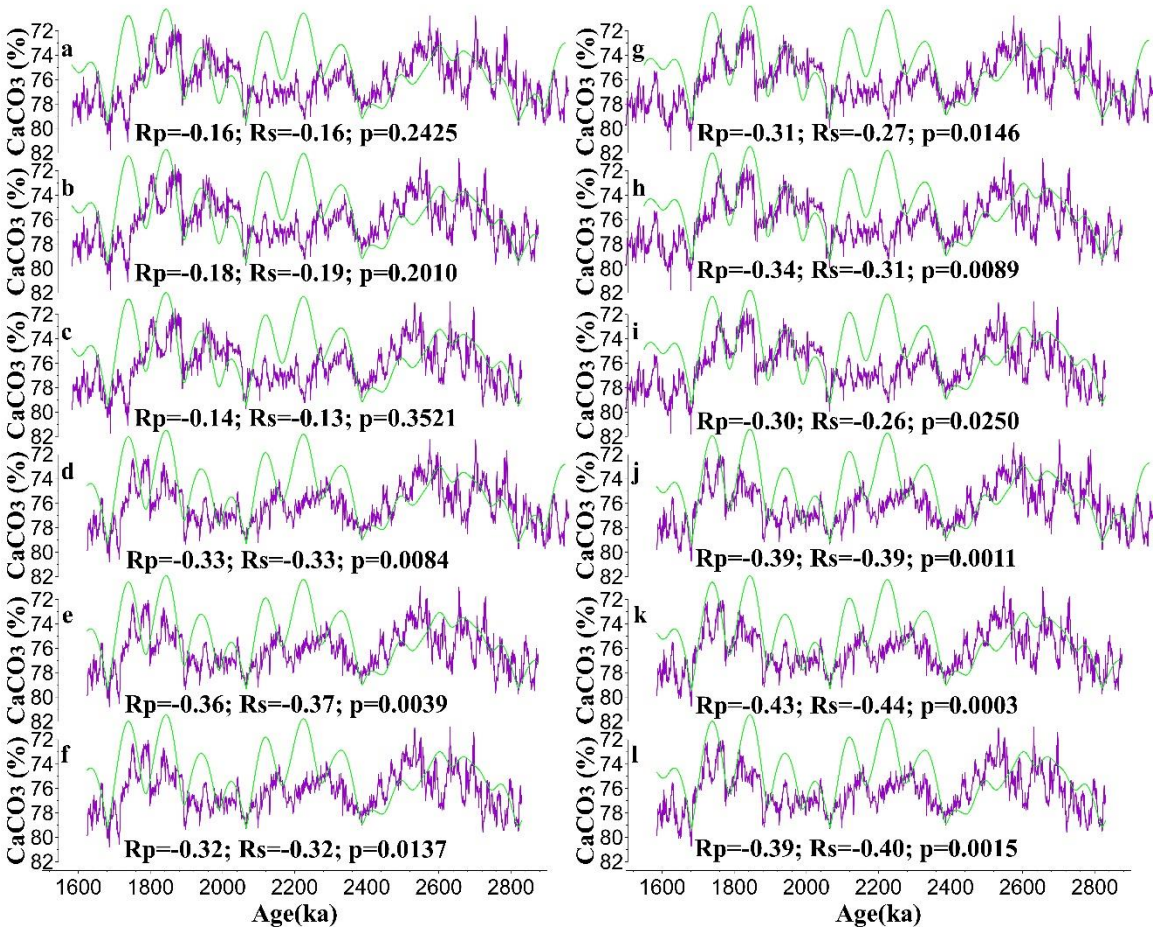

Figure S5. Alternative tunings for Site U1464 to eccentricity. Four eccentricity minima at 1682, 2066, 2388 and 2821 kyr are tuning targets for 12 potential $CaCO_3$ maxima. See Table S4 for tie-point depths used in (a)-(l). Option (k) is the choice in this study. Purple (green) lines represent $CaCO_3$ (eccentricity) records. Rp (Rs) represents Pearson (Spearman) correlation coefficient (see Text S1).

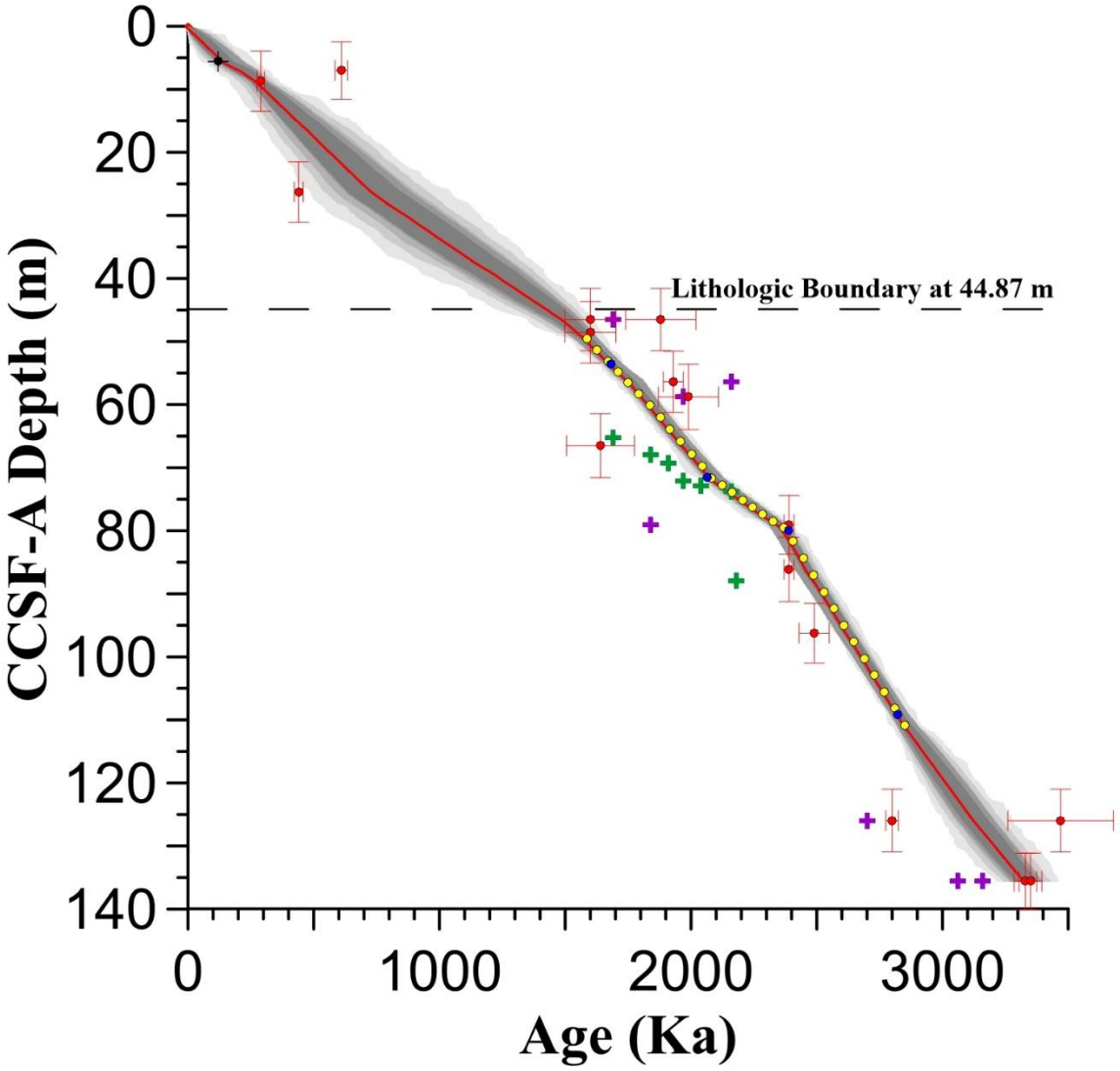

Figure S6. Same as main-text figure 2b, with additional age-depth markers for comparison. Green crosses are inferred chrono-stratigraphy for Site U1464 based on tie-points between U1463 and U1464 using dynamic time warping of natural gamma radiation records (Groeneveld et al., 2021). Purple crosses are revised biostratigraphic datums for neighboring Site U1463 from Groeneveld et al., 2021.

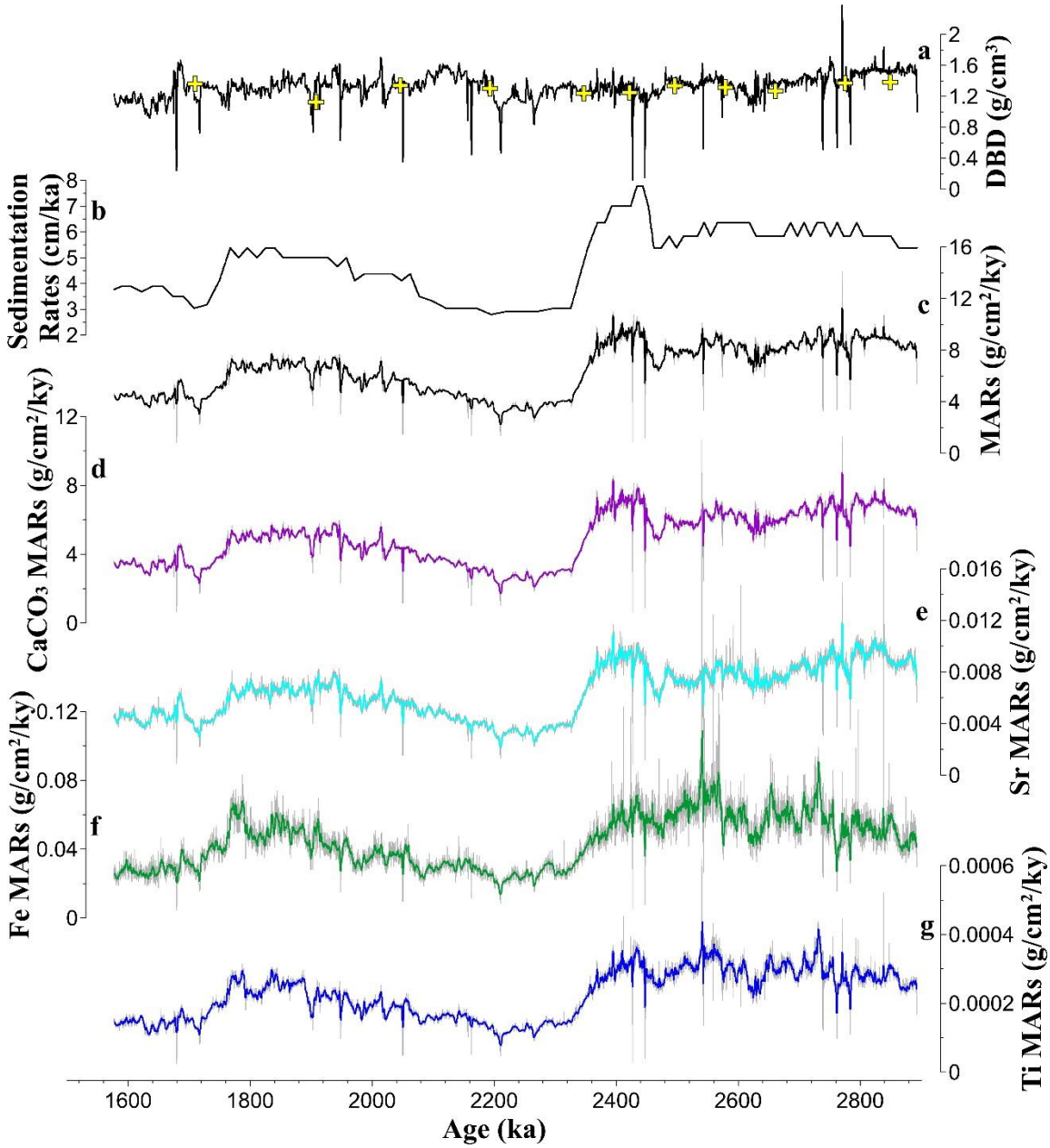

Figure S7. IODP Site U1464 sediment dry bulk density (DBD; black = calculated, yellow = shipboard measurements (Gallagher et al., 2017a), a), sedimentation rates (b) and mass accumulation rates (MARs) over ~1.6-2.9 Ma. Total MARs (c); $CaCO_3$ MARs (d); Sr MARs (e); Fe MARs (f) and Ti MARs (g). Bold lines (grey lines) in c-g are 21-point running averages (original data).

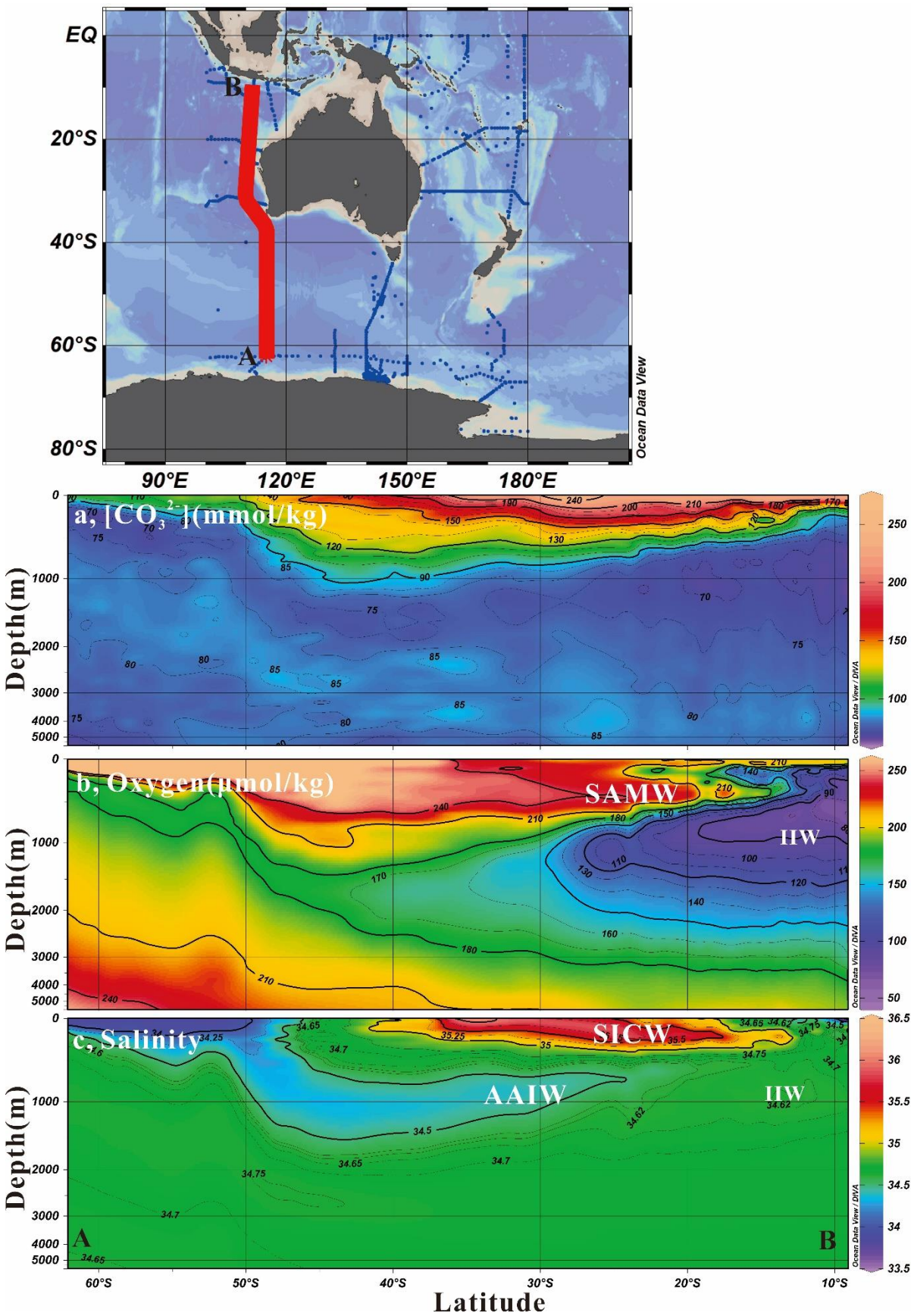
EQ
20°S
40°S
60°S
80°S
90°E
120°E
150°E
180°E
B
A
Ocean Data View
a, [CO3 2-](mmol/kg)
b, Oxygen(μmol/kg)
SAMW
IIW
c, Salinity
SICW
AAIW
IIW
Depth(m)
Latitude
60°S
50°S
40°S
30°S
20°S
10°S
A
B
Ocean Data View / DIVA

Figure S8. Meridional cross-section profiles of (a) $[CO_3^{2-}]$, (b) oxygen content and (c) salinity for transect-AB (red line). Data is from the GLODAPv2.2021 dataset (Key et al., 2015). $[CO_3^{2-}]$ from the GLODAPv2.2021 dataset is calculated using the CO2SYS method (Lewis & Wallace, 1998). Blue dots represent available data-points. SAMW: Sub-Antarctic Mode Water; AAIW: Antarctic Intermediate Water; SICW: South Indian Central Water; IIW: Indonesian Intermediate Water. SAMW is characterized by high-oxygen content (Herraiz-Borreguero & Rintoul, 2011; Woo & Pattiaratchi, 2008); AAIW is characterized by a salinity minimum (Wong, 2005; Woo & Pattiaratchi, 2008); SICW is characterized by a salinity maximum (Woo & Pattiaratchi, 2008); IIW is characterized by a salinity minimum (Talley & Sprintall, 2005) and an oxygen minimum (Fieux et al., 1996).

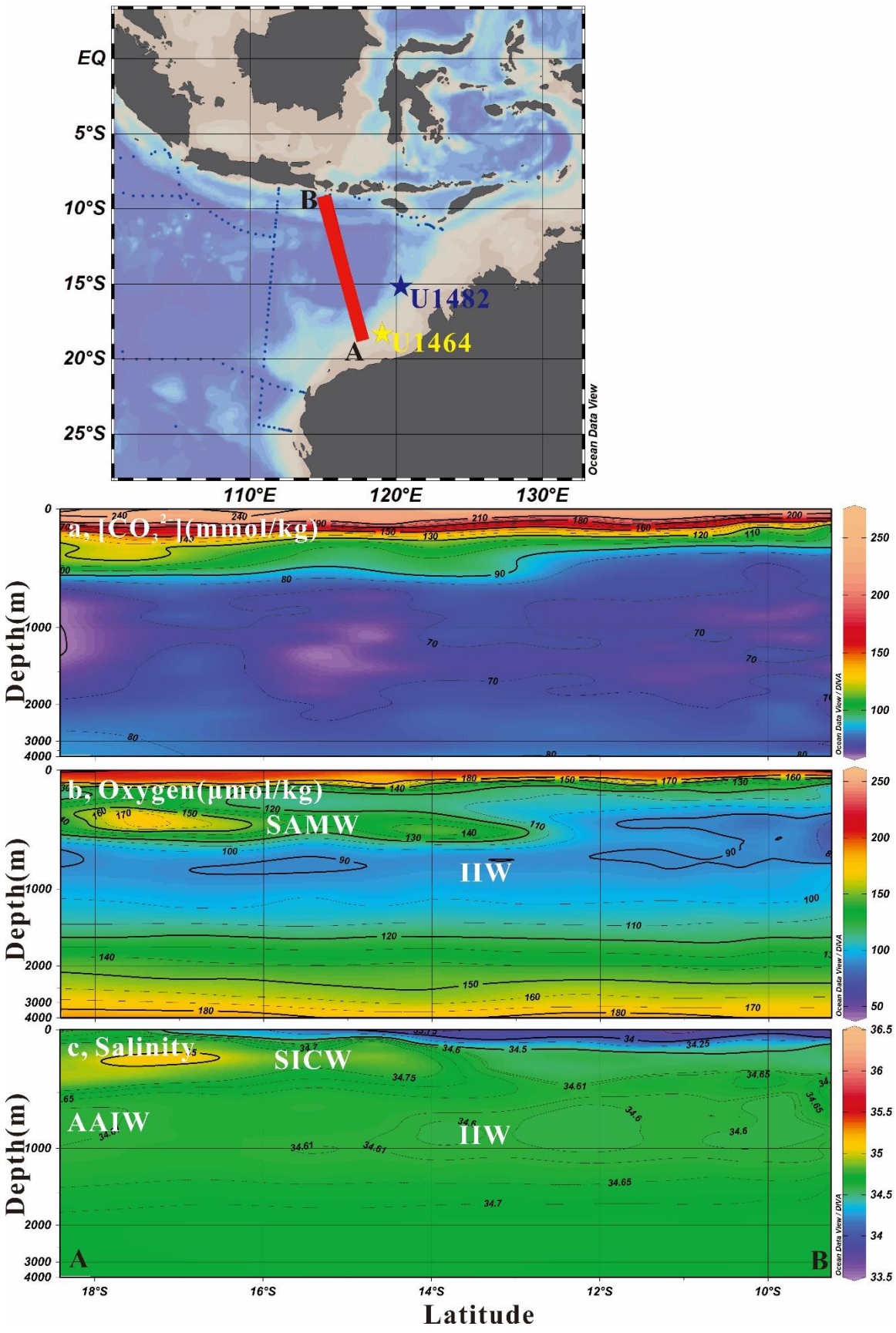
EQ
5°S
10°S
15°S
20°S
25°S
110°E
120°E
130°E
B
A
U1482
U1464
Ocean Data View
a, [CO3 2-](mmol/kg)
b, Oxygen(μmol/kg)
SAMW
IIW
c, Salinity
SICW
AAIW
IIW
Depth(m)
0
1000
2000
3000
4000
Ocean Data View / DIVA
250
200
150
100
50
36.5
36
35.5
35
34.5
34
33.5
A
B
18°S
16°S
14°S
12°S
10°S
Latitude

Figure S9. Meridional cross-section profiles of (a) $[CO_3^{2-}]$, (b) oxygen content and (c) salinity for transect-AB (red line). Yellow (blue) star marks IODP Site U1464 (U1482). This cross-section is the closest GLODAPv2.2021 data to Site U1464 and Site U1482. $[CO_3^{2-}]$ from the GLODAPv2.2021 dataset is calculated using the CO2SYS method (Lewis & Wallace, 1998). Blue dots represent available data-points. SAMW: Sub-Antarctic Mode Water; AAIW: Antarctic Intermediate Water; SICW: South Indian Central Water; IIW: Indonesian Intermediate Water. SAMW is characterized by high-oxygen content (Herraiz-Borreguero & Rintoul, 2011; Woo & Pattiaratchi, 2008); AAIW is characterized by a salinity minimum (Wong, 2005; Woo & Pattiaratchi, 2008); SICW is characterized by a salinity maximum (Woo & Pattiaratchi, 2008); IIW is characterized by a salinity minimum (Talley & Sprintall, 2005) and an oxygen minimum (Fieux et al., 1996).

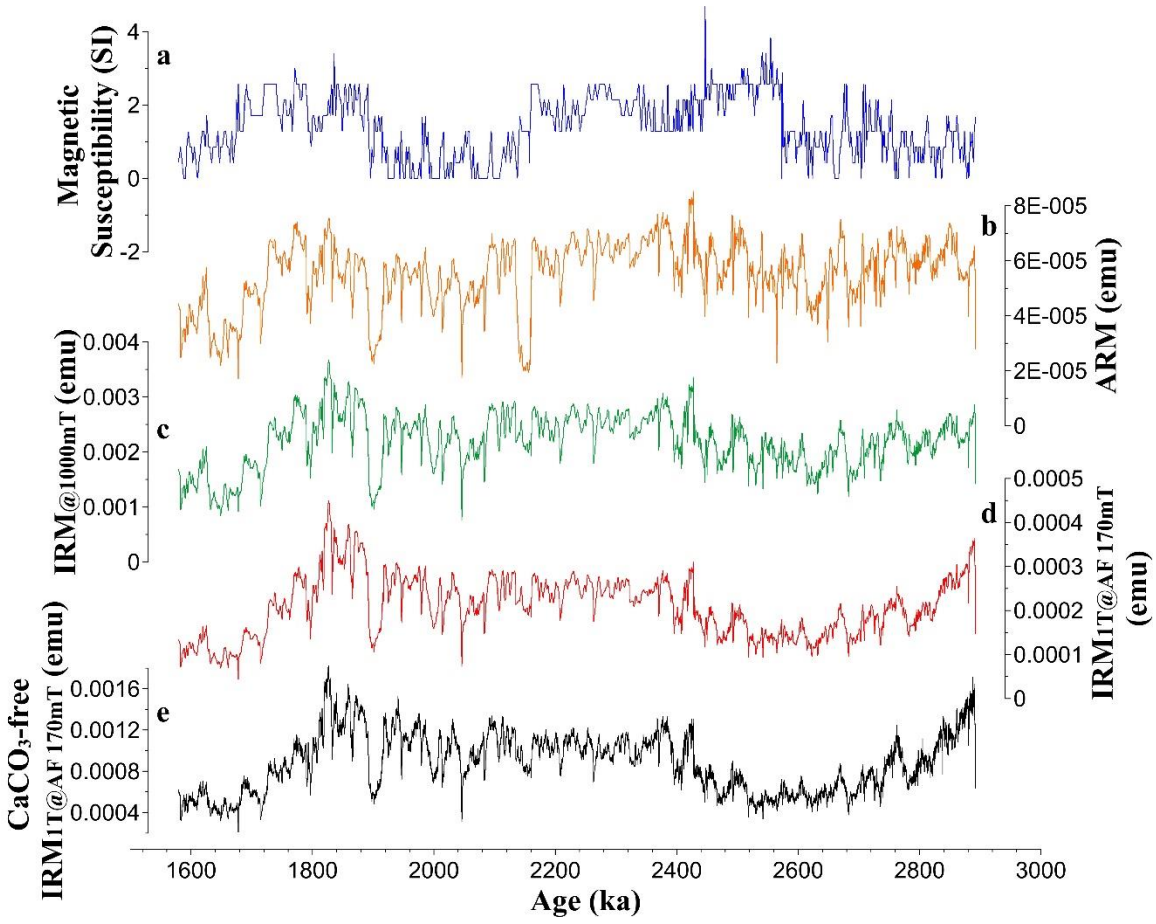

Figure S10. IODP Site U1464 magnetic parameters over the late Pliocene/early Pleistocene. (a) Magnetic susceptibility; (b) ARM; (c) $IRM_{@1000mT}$; (d) $IRM_{1T@AF\ 170mT}$ and (e) $CaCO_3$-free $IRM_{1T@AF\ 170mT}$. Magnetic susceptibility data is from Gallagher et al., 2017a and other data are measured in this study.

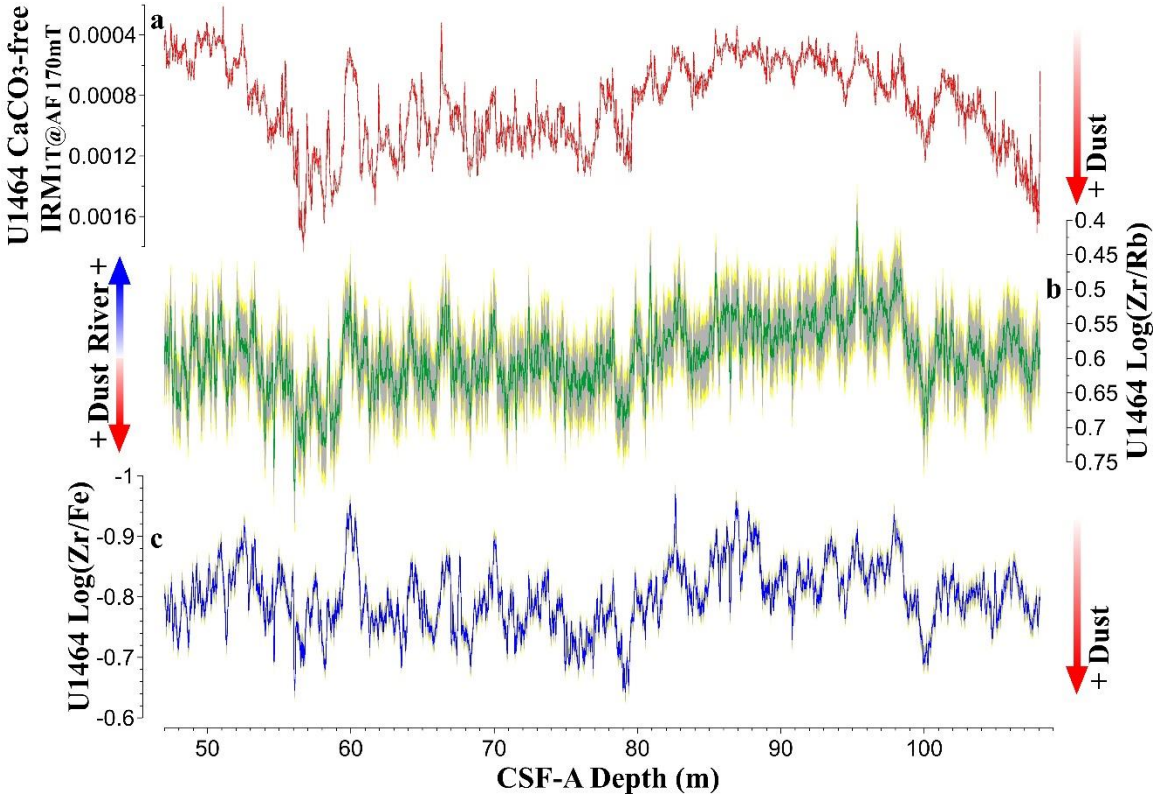

Figure S11. Dust proxy records from the Australian NWS and their uncertainties. $CaCO_3$-free $IRM_{1T@AF\ 170mT}$ (a, red), Log(Zr/Rb) (b, green: 21-point running average), and Log(Zr/Fe) (c, blue: 21-point running average) records at Site U1464. The grey and yellow shadings represent the 95 % and 99 % confidence intervals. Uncertainty calculations for these three dust records are shown in Text S2.

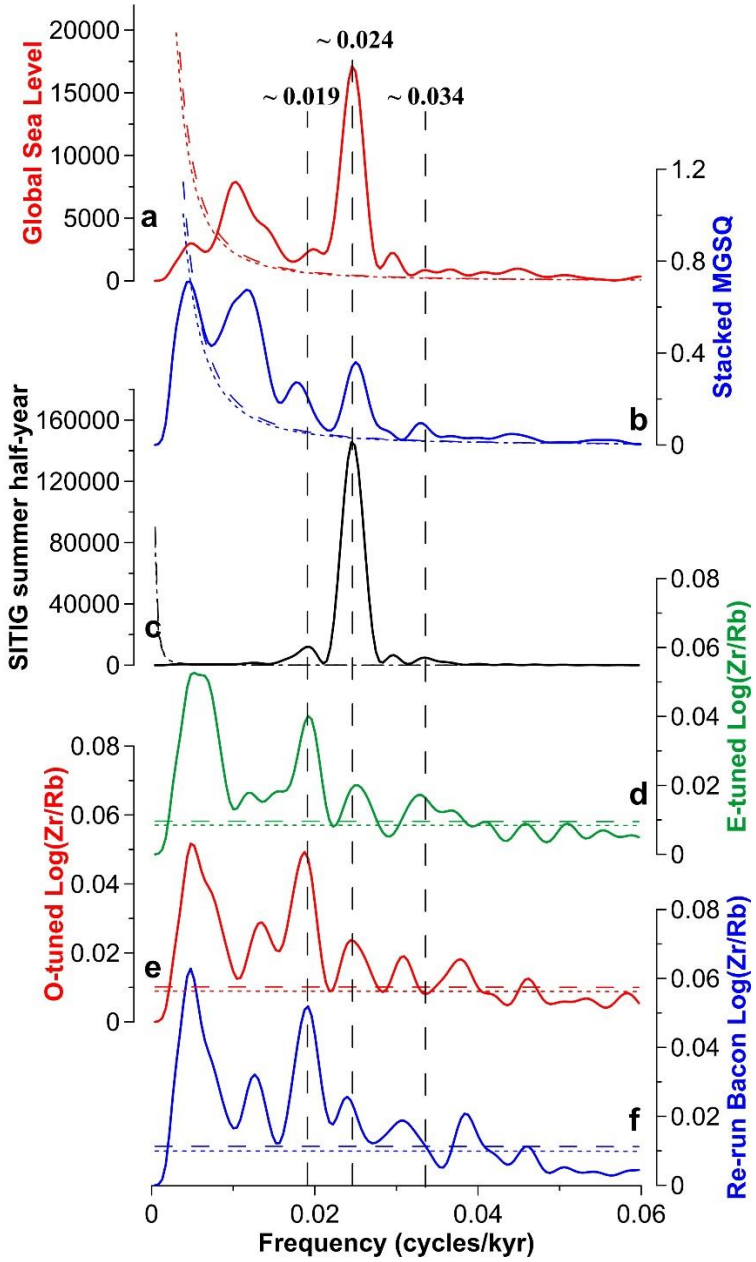

Figure S12. Spectral analyses of Northwest Australian dust fluxes and its three potential origins over the 1.6-2.9 Ma interval using the Redfit method. Power spectra for global sea level (Rohling et al., 2021) (a), stacked mean grain-size of quartz (MGSQ) from the Chinese Loess Plateau (Sun et al., 2006) (b), inter-tropical insolation gradient (SITIG) summer half-year (Laskar et al., 2004) (c), and Site U1464 Log(Zr/Rb) on the eccentricity tuning age model (d), obliquity tuning age model (e) and re-run Bacon age model (f). The Redfit spectra (oversample = 8, segment = 8) and confidence levels (90%, dashed; 95%, dot) are shown.

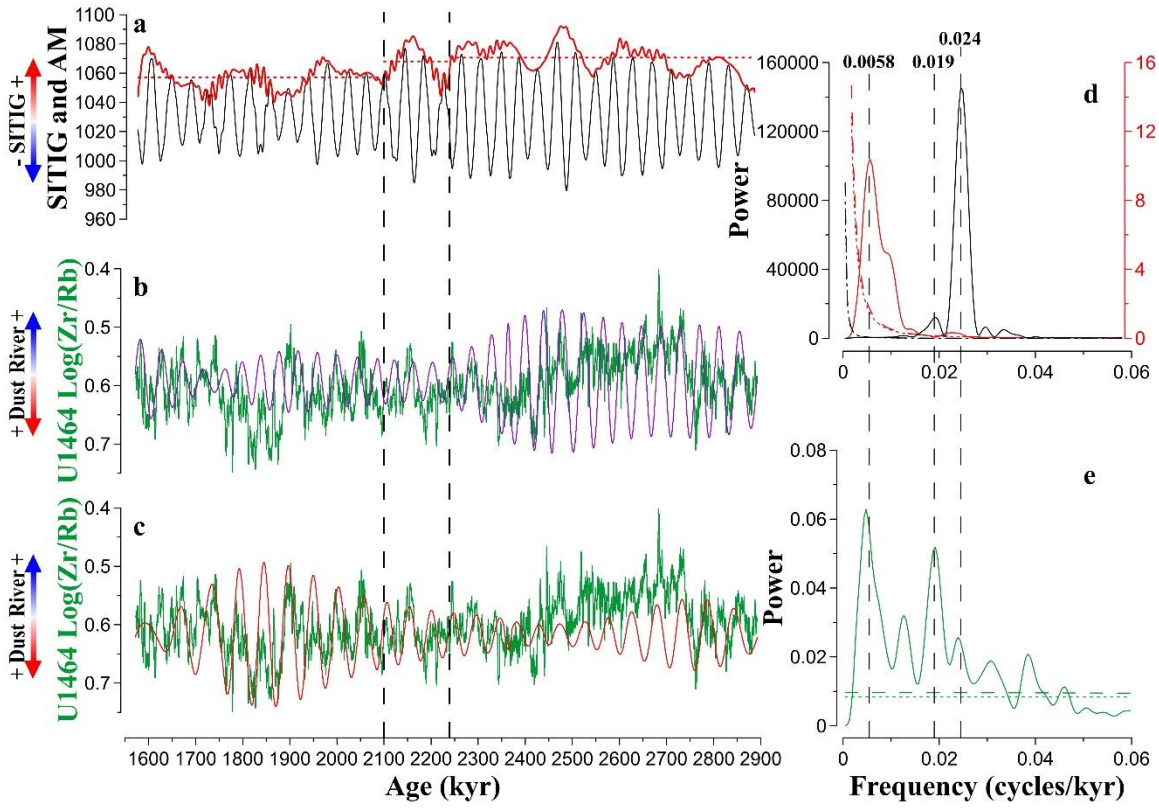

Figure S13. Inter-tropical insolation gradient (SITIG) summer half-year (black) and its amplitude modulation (AM, red) (a); Site U1464 Log(Zr/Rb) (green) and its 0.023-0.027 filter (purple) (b) and 0.017-0.021 filter (red) (c); Redfit power spectra of SITIG summer half-year (black) and its AM (red) (d), and Site U1464 Log(Zr/Rb) (green) (e). The SITIG summer half-year AM envelope is calculated using the MATLAB built-in function "hilbert" (Hilbert transform), and the mean values before 2.24 Ma, during 2.24-2.1 Ma and after 2.1 Ma are shown as red dotted lines in a. The Log(Zr/Rb) filters are calculated using the Fast Fourier transform in the Origin software package. Confidence levels (90%, dot; 95%, dashed) and significant frequencies (dash lines) in d and e are shown.

Table S1. Results of ICP-OES analysis for Site U1464, and standard deviation (SD) for certified reference materials (marine sediments BCSS-1, MESS-1 and estuarine sediments 1646).

Hole, Core, Section, Depth	CSF-A Depth/m	Ca/ppm	Fe/ppm	Sr/ppm	Ti/ppm
D1H1 36-37 cm	0.36	271791.19	2521.55	2385.06	8.46
D1H2 109-110 cm	2.59	260929.47	1891.64	2620.27	8.93
D2H1 78-79 cm	4.28	243912.04	2708.33	2666.67	10.92
D2H2 149-150 cm	6.49	271530.51	3100.39	2066.93	15.15
D2H4 1-2 cm	8.01	242292.39	3117.85	1685.73	20.90
D2H6 17-18 cm	11.17	268626.98	1958.71	1469.04	11.78
D2H7 65-66 cm	12.87	273355.58	2287.89	1572.93	18.33
D3H1 144-145 cm	14.44	273812.92	2592.59	1709.40	19.63
D3H3 142-143 cm	17.42	280691.51	2599.91	1630.00	16.60
D3H4 144-145 cm	18.94	281755.47	2911.51	1669.84	21.47
D3H5 140-141 cm	20.4	279954.03	2742.59	1685.39	14.13
D3H7 53-54 cm	22.05	267369.15	2869.38	1611.86	17.42
D4H2 70-71 cm	24.7	233333.33	2835.28	1516.03	20.79
D4H3 62-63 cm	26.12	277248.93	1934.79	1956.21	9.27
D4H4 149-150 cm	28.49	209504.90	2115.83	1793.55	12.91
D4H5 77-78 cm	29.27	255956.59	2067.14	1696.11	15.20
D4H7 60-61 cm	32	251155.27	1975.51	1802.22	17.37
D5H2 117-118 cm	34.67	290882.92	2252.88	2000.96	18.25
D5H4 18-19 cm	36.68	265655.62	2183.85	1973.87	17.46
D5H6 20-21 cm	39.7	250397.20	1528.04	1808.41	13.95
D5H7 56-57 cm	41.56	258108.11	1657.82	1636.10	12.50
D6H2 1-2 cm	43.01	272419.43	2340.03	1751.52	11.83
D6H3 0-1 cm	44.5	243153.92	4185.55	1458.92	26.35
D6H3 53-54 cm	45.03	285259.99	4712.08	1469.70	25.45
D6H4 56-57 cm	46.56	275391.50	6590.60	1315.44	35.50
D6H4 146-147 cm	47.46	210471.83	5069.81	794.42	25.83
D6H5 87-88 cm	48.37	280966.42	7023.59	952.81	30.72
D6H6 61-62 cm	49.61	265960.04	6374.27	994.15	23.82
D6H6 147-148 cm	50.47	248979.10	6504.62	1035.49	25.33
D7H1 80-81 cm	51.8	231312.17	7162.48	952.16	40.03
D7H2 5-6 cm	52.55	252171.95	8748.87	1004.52	42.15
D7H3 1340 cm	55.34	213450.02	6729.62	967.30	33.98
D7H4 147-148 cm	56.97	212837.54	6752.99	956.18	39.73
D7H6 59-60 cm	59.09	221516.96	7328.14	1044.91	36.04
D8H1 145-146 cm	61.95	260158.80	6130.31	1106.96	30.97
D8H3 2-3 cm	63.52	220878.58	5671.27	1036.53	36.44
D8H3 145-146 cm	64.95	234390.13	6512.58	1030.98	26.85
D8H6 1-2 cm	68.01	231451.21	5742.94	1054.98	22.78
D8H7 27-28 cm	69.77	215530.67	7339.34	1051.61	39.01
D9H2 117-118 cm	72.67	241003.83	6201.62	918.76	26.98
D9H4 17-18 cm	74.67	225276.83	5704.86	983.82	31.78
D9H5 2-3 cm	76.02	235133.89	5090.03	886.43	33.07
D9H6 81-82 cm	78.31	240009.40	7066.29	902.68	23.95
D10H1 100-101 cm	80.5	208100.83	6549.19	1027.90	43.27
D10H3 42-43 cm	82.92	173891.74	8224.45	1119.93	46.95
D10H5 34-35 cm	85.84	212358.44	7304.28	945.35	33.46
D11H2 8-9 cm	90.58	208958.62	5463.85	886.77	30.76
D11H5 28-29 cm	95.28	253995.27	7751.77	1078.01	47.50
D12H1 140-141 cm	99.9	227825.89	4956.70	1011.85	42.33
D12H5 101-102 cm	105.51	203052.39	5207.29	997.72	37.78
Certified Reference Materials	**Replicates Count**	**Ca SD**	**Fe SD**	**Sr SD**	**Ti SD**
1646	4	3.422‰	1.064‰	0.008‰	0.004‰
BCSS-1	3	4.981‰	2.607‰	0.009‰	0.005‰
MESS-1	3	2.445‰	2.792‰	0.004‰	0.022‰
Average Value	---	3.616‰	2.154‰	0.007‰	0.010‰

Table S2. IODP Site U1464 shipboard $CaCO_3$ measurements (Gallagher et al., 2017a), scanning-XRF Ln(Ca/Fe) values, and predicted $CaCO_3$ content.

Hole, Core, Section	CSF-A Depth/m	$CaCO_3$/%	Ln(Ca/Fe)	Predicted $CaCO_3$/%
B1H1	1.45	89.91	4.693	92.35
B3H3	16.15	88.42	4.140	87.05
B4H3	25.55	87.32	4.207	87.70
B5H4	36.68	88.57	4.213	87.75
B6H3	44.65	87.30	3.839	84.17
B7H3	54.15	73.45	2.746	73.70
B7H3	63.65	75.90	3.062	76.72
B7H3	73.15	72.72	2.949	75.64
B7H3	82.65	76.31	2.784	74.07
B7H3	92.15	74.59	3.164	77.70
B7H3	101.65	79.38	3.093	77.03

Table S3. Age control-points (Gallagher et al., 2017a) in our Site U1464 Bacon age model. CN: calcareous nannofossils; PF: planktonic foraminifers; Base: first appearance depth; Top: last appearance depth. The CCSF-A for each point is calculated from their middle CSF-A depth, based on the established linear relationship between CSF-A and CCSF-A (Gallagher et al., 2017a).

Hole, Core, Section	Depth CSF-A (m)	Depth CCSF-A (m)	Marker Species	Type	Age (Ma)
Core Top	0	0	---	---	0
U1464D-1H-CC	3.55	8.72	Base E. huxleyi	CN	0.29
U1464B-2H-CC	11.51	7.02	Top G. tosaensis	PF	0.61
U1464B-4H-CC	30.82	26.28	Top P. lacunosa	CN	0.44
---	43.00	44.87	Lithologic Boundary	---	---
U1464B-6H-CC	49.82	46.53	Top C. macintyrei	CN	1.6
U1464B-6H-CC	49.82	46.53	Top G. fistulosus	PF	1.88
U1464B-6H-CC	49.82	56.37	Base G. truncatulinoides	PF	1.93
U1464D-6H-CC	51.33	48.54	Top C. macintyrei	CN	1.6
U1464B-7H-CC	59.46	56.37	Top D. brouweri	CN	1.93
U1464D-7H-CC	60.84	58.78	Top G. extremus	PF	1.99
U1464B-8H-CC	69.09	66.51	Top G. apertura	PF	1.64
U1464D-9H-CC	79.83	79.04	Top G. limbata	PF	2.39
U1464B-10H-CC	88.17	86.14	Top D. pentaradiatus	CN	2.39
U1464B-11H-CC	97.42	96.23	Top D. surculus	CN	2.49
U1464B-14H-CC	126.30	125.96	Top D. tamalis	CN	2.8
U1464B-14H-CC	126.30	135.59	Base G. fistulosus	PF	3.33
U1464B-14H-CC	126.30	135.59	Base G. tosaensis	PF	3.35
U1464B-14H-CC	126.30	125.96	Top D. altispira	PF	3.47

Table S4. Different depth options for each Site U1464 $CaCO_3$-to-eccentricity tie-point (see Figure 4; Figure S5). Twelve possible combinations are shown (Figure S5). Bold numbers represent the best option for the U1464 age model in this study, based on visual alignment and correlation analysis between eccentricity and U1464 $CaCO_3$.

Eccentricity Tuning-point	Tuning Age (kyr)	Depth (m CCSF-A)	Bacon Age (kyr)
1	1682	51.99	1746
1	**1682**	**53.62**	**1800**
2	2066	63.05	2012
2	**2066**	**71.57**	**2174**
3	**2388**	**79.97**	**2332**
4	2821	104.91	2738
4	**2821**	**109.18**	**2817**
4	2821	112.22	2873

Table S5. IODP Site U1464 tuning tie-points.

Depth (m CCSF-A)	Initial Bacon Age (kyr)	Tuning Age (kyr)	Reference proxy	Orbital Target
49.53	1664	1587	Log(Zr/Rb)	Obliquity
51.33	1725	1627	Log(Zr/Rb)	Obliquity
53.14	1784	1672	Log(Zr/Rb)	Obliquity
53.62	1800	1682	$CaCO_3$	Eccentricity
54.85	1841	1709	Log(Zr/Rb)	Obliquity
56.52	1892	1750	Log(Zr/Rb)	Obliquity
58.28	1926	1793	Log(Zr/Rb)	Obliquity
60.10	1958	1837	Log(Zr/Rb)	Obliquity
62.00	1993	1878	Log(Zr/Rb)	Obliquity
63.93	2028	1917	Log(Zr/Rb)	Obliquity
65.88	2063	1959	Log(Zr/Rb)	Obliquity
67.80	2100	2002	Log(Zr/Rb)	Obliquity
69.80	2139	2044	Log(Zr/Rb)	Obliquity
71.57	2174	2066	$CaCO_3$	Eccentricity
71.71	2177	2081	Log(Zr/Rb)	Obliquity
72.82	2198	2124	Log(Zr/Rb)	Obliquity
73.94	2220	2164	Log(Zr/Rb)	Obliquity
75.14	2244	2205	Log(Zr/Rb)	Obliquity
76.30	2266	2246	Log(Zr/Rb)	Obliquity
77.41	2288	2284	Log(Zr/Rb)	Obliquity
78.48	2309	2327	Log(Zr/Rb)	Obliquity
79.55	2327	2368	Log(Zr/Rb)	Obliquity
79.97	2332	2388	$CaCO_3$	Eccentricity
81.61	2354	2405	Log(Zr/Rb)	Obliquity
84.35	2390	2448	Log(Zr/Rb)	Obliquity
87.06	2429	2487	Log(Zr/Rb)	Obliquity
89.749	2473	2528	Log(Zr/Rb)	Obliquity
92.36	2515	2569	Log(Zr/Rb)	Obliquity
95.05	2559	2607	Log(Zr/Rb)	Obliquity
97.64	2604	2649	Log(Zr/Rb)	Obliquity
100.28	2653	2690	Log(Zr/Rb)	Obliquity
102.90	2701	2728	Log(Zr/Rb)	Obliquity
105.52	2750	2768	Log(Zr/Rb)	Obliquity
108.21	2799	2810	Log(Zr/Rb)	Obliquity
109.18	2817	2821	$CaCO_3$	Eccentricity
110.88	2848	2851	Log(Zr/Rb)	Obliquity